Supplementary Information for: Locally enhanced precipitation organized by planetary-scale waves on Titan

Jonathan L. Mitchell,[1*] Máté Ádámkovics,[2]
Rodrigo Caballero,[3,4] Elizabeth P. Turtle[5]

[1]Earth & Space Sciences, Atmospheric & Oceanic Sciences
University of California, Los Angeles, CA 90095, USA
[2]Astronomy Department, University of California, Berkeley, CA 94720, USA
[3]Department of Meteorology (MISU), Stockholm University, Stockholm, Sweden
[4]Bert Bolin Center for Climate Research, Stockholm University, Stockholm, Sweden
[5]Johns Hopkins University, Applied Physics Laboratory, Laurel, MD 20723, USA

1 Method for producing simulated cloud observations from GCM precipitation

Radiative Transfer

Images of Titan's clouds have been interpreted as regions of moist convection and used to study circulation in the lower atmosphere. We describe a methodology for using the output from the circulation models described here to predict cloud morphologies. The simulated images are compared with observations from Cassini/ISS at a wavelength, λ=938 nm.

Base model

The atmospheric temperature, pressure, and composition are setup according to our previous radiative transfer model ([1] and references therein). This model has been used to study cloud morphologies and spectra[2]. The difference here is that we use the most recently reported methane gas opacities[3] and adopt the aerosol scattering properties and vertical (altitude) opacity structure used to interpret measurements made by the Huygens probe[4]. We fit 0.935 μm phase functions[4] with high order Legendre polynomials (Figure S1), and use the discrete ordinates method (DISORT) with 48 streams to solve the radiative transfer. A Cassini/ISS map (http://ciclops.org, PIA11149) of the surface at 938nm is used as an input for the surface reflectivity, stretched between values of 1 – 25%, consistent with the ∼16% reflectivity measured at the Huygens landing site. Similarly, a 619nm image is calculated using the aerosol scattering phase function reported at 600nm. This wavelength is insensitive to the surface or atmosphere below 100km and is used for simulation of the Cassini/ISS image processing[5].

Cloud Scattering

We calculate the scattering properties of a cloud that is defined by a distribution of spherical liquid methane droplets. For droplets of radius, r, the particle size distribution, $n(r)$ is given by

$$n(r) \propto r^6 \exp(-6r/r_m) \tag{1}$$

We pick r_m and scale the distribution to correspond with the microphysical models of methane clouds[6]. Our particle size distribution is illustrated in Figure S2. The total particle number density, $N = \int_0^\infty n(r)dr$, is used to define the normalized size distribution function,

$$\bar{n}(r) = \frac{n(r)}{N} \tag{2}$$

which determines the fraction of particles in a given bin, $\bar{n}(r)dr$. The ensemble properties of the particle distribution are the weighted sum of properties at a given radius. For example, we calculate Mie scattering phase functions, $p_r(\theta)$, and single-scattering albedos, ω_r, for particle radii throughout the range r_0=0.001 μm to R= 4000 μm, and determine the scattering phase function of the distribution as

$$p(\theta) = \sum_{r=r_0}^{R} p_r(\theta)\bar{n}(r)dr \tag{3}$$

Similarly, the weighed sum of ω_r is used to calculate the single scattering albedo of the distribution, ω.

Cloud optical depths

The daily average precipitation from the GCM is used to calculate the cloud opacity. The cloud optical depth is given by $\tau = \kappa z$ where z is a path length through the cloud and the extinction coefficient, κ, for the distribution is given by

$$\kappa = \int_0^R \pi r^2 Q_{\text{ext}} n(r)dr \tag{4}$$

We assume the geometric limit of scattering such that, Q_{ext}=2, and substitute the normalized distribution function to get the optical depth

$$\tau = 2\pi N z \int_0^R \bar{n}(r)r^2 dr \tag{5}$$

If we assume the distribution with altitude is uniform, the total mass of liquid methane per unit area in a column of height, z, (density, ρ=0.422 g/cm^3) is given by

$$M = \frac{4\pi}{3}\rho N z \int_0^R \bar{n}(r)r^3 dr \tag{6}$$

We can now define the cloud optical depth for a given distribution that arises from a mass of precipitable methane independent of N and z,

$$\tau/M = \frac{3}{2\rho}\left[\left(\int_0^R \bar{n}(r)r^2 dr\right) / \left(\int_0^R \bar{n}(r)r^3 dr\right)\right] \tag{7}$$

For our particle size distribution (Equation 1), numerical integration gives $\tau/M = 5.2\text{m}^2/\text{kg}$. Assuming monodisperse 512 μm particles gives τ/M=6.9 m^2/kg. For the typical precipitation events

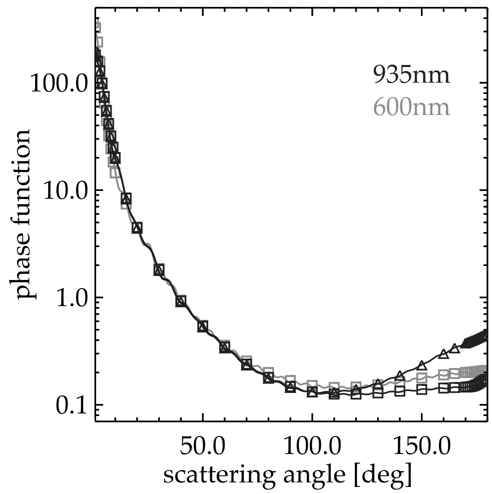

Figure S1: Aerosol scattering phase functions at 600nm and 935nm reported by [4]. Scattering at 935 nm reported for regions above and below 80 km (black squares and triangles, respectively). Aerosol scattering at 600nm, used to simulate Cassini/ISS image processing in [5], is sensitive to the atmosphere above 100km, and a single phase function is reported (grey squares). The best fit 64th and 48th order Legendre polynomials (solid lines) are used to fit the phase functions at 600nm and 935nm. High order polynomials are required to fit the strongly forward-scattering phase functions.

shown in Figures 1 and 2 of the main text (e.g., the chevron feature) the precipitation rate of $1.2{\times}10^{-5}$ kg/m^2/s equates to $M \sim 1$ kg/m^2 when integrated over the GCM timestep of 1 day. If ∼10–20% of the precipitable moisture is in cloud droplets (consistent with terrestrial clouds), then the chevron feature from the precipitation field in the GCM results in an optically thick cloud feature in the simulated observations.

Clouds of frozen methane

[7] used a steady-state condensation model with the Voyager temperature profile to predict that clouds would be composed of liquid droplets below ∼12 km and solid crystals above. The shape of the crystals could be octahedral or cubic, as suggested for solar system ices in general by [8]. The vapor-pressure of methane measured by the Huygen's probe was used to calculate the relative humidity of methane over mixed methane-nitrogen cloud droplets and solid methane cloud particles by [9]. These results suggested a 'sub-visible' liquid methane-nitrogen cloud below ∼16 km and a cloud of solid methane extending from 20–40 km.

The time-dependent cloud microphysical model of [6] considered the condensation of methane onto ethane coated hydrocarbon aerosol (haze) particles. This followed their earlier work on the heterogenous nucleation of ethane onto aerosol particles and ethane cloud formation [10]. In their model, methane nucleates onto an ethane cloud particle creating an ice crystal, which serves as the condensation nucleus for addition methane or ethane creating 'mixed' clouds. The crystals are significantly smaller than the methane droplets. Our particle size distribution, with a peak at

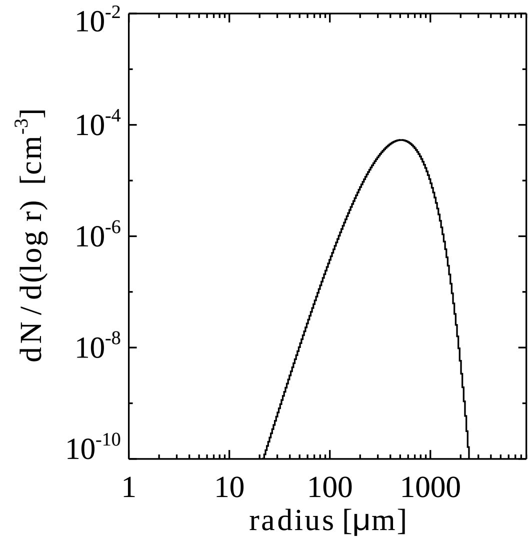

Figure S2: A cloud particle size distribution with r_m=512 μm is broadly consistent with methane clouds at 10–20 km predicted by Barth & Toon, 2006.

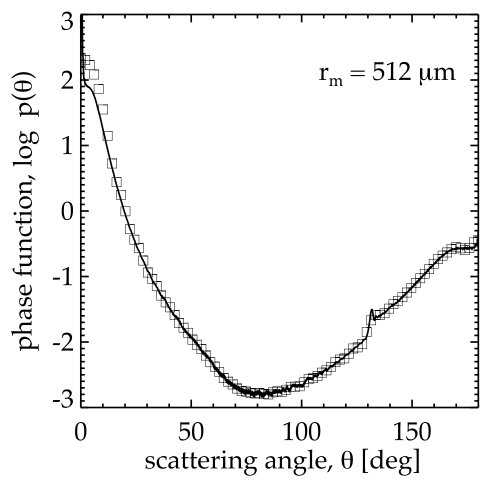

Figure S3: Cloud scattering phase function at λ=938 nm for a distribution of spherical droplets (*solid curve*), and the best fit 48^{th} order Legendre polynomial (*squares*). Optical constants for liquid methane, n_r=1.288 and n_i= 1.1×10^{-6}. The value for n_i has been linearly interpolated between data reported at 888.5 nm and 974.2 nm. The single scattering albedo, ω, for the cloud is $\sim$1 since $4\pi n_i r_m/\lambda \ll 1$.

r_m=512 μm is consistent with their base model for mixed methane-ethane clouds at 20 km, and intermediate between the two size distributions of pure methane cloud particles calculated at 10 and 20 km.

[6] consider various particle compositions and barriers to nucleation, and show how the size distributions change with altitude and time. Based on the Huygens temperature profile, methane freezes above 16 km in their model, nitrogen is exsolved during this process, and pure methane crystals remain. In all cases the droplet sizes decrease with altitude from 10 to 30 km. At 30 km the size distribution peaks near 100 μm, with a significant fraction of particles in the several micron range.

While we can speculate about the scattering of methane ice particles in clouds, there is a fundamental limitation in the lack of knowledge of the solid particle morphology. Considering our particle size distribution with the refractive indices of solid methane (n_r=1.313 and n_i=0.0) in place of liquid methane results in an insignificant change to $p(\theta)$ or ω and causes an $\sim$2% increase in cloud albedo. Considering the particle size distribution at 30 km, with r_m =128 μm, results in a slightly less forward-scattering phase function and an increase in cloud albedo of $\sim$4%. However, the assumption of solid, spherical, methane 'marbles' serves only as an illustration. A more important impact of the smaller particle size distribution at high altitudes is that τ/M increases by a factor of $\sim$4, somewhat compensated by the increased density of solid methane (0.519 g/cm^3), which decreases τ/M by $\sim$20%. Thus, there are a few reasons to believe that scattering from clouds of solid methane particles would likely lead to somewhat brighter clouds in our model. However, this would not change any aspect of our results, and would remain consistent with the observations, because the fraction of precipitable methane in clouds is uncertain and could reasonably be smaller than the terrestrial value of 10-20%.

2 Description of the Titan GCM

Our Titan GCM is based on the previously developed model[11]. The model integrates the dry primitive equations of motion of an ideal gas on a sphere using a spectral method [12] at T21 resolution (64 longitudes, 32 latitudes) and on 20 vertical levels spaced evenly in pressure from 0 to 1500 hPa. Simplified treatments of radiation, convection, and boundary-layer processes are included as follows:

- *Radiation:* A two-stream approximation is used with grey infrared opacities to solve for infrared radiative transfer. The total infrared optical depth, $\tau_\infty = 9$. Reflection and absorption of shortwave is treated parametrically to simulate these effects[13]. The seasonal cycle of insolation is fully accounted for. We neglect the diurnal cycle.

- *Convection:* Moist convection of methane is modeled using a "simplified Betts-Miller" scheme[14]. There are only two parameters of the model, the relative humidity to which convection relaxes and a relaxation timescale. These are fixed at 80% and 2 hours, respectively. Saturation of methane is diagnosed by the Claussius-Clapeyron equation assuming pure methane.

- *Boundary layer:* The boundary layer implements a simplified Monin-Obukhov similarity theory that accounts for the rectification of turbulent fluxes in statically stable conditions[14].

The model surface is a uniform slab of specified heat capacity equivalent to the "porous icy regolith" used in a previous study[15]. Methane is assumed to exist in infinite supply at the surface so that evaporation occurs wherever conditions are favorable.

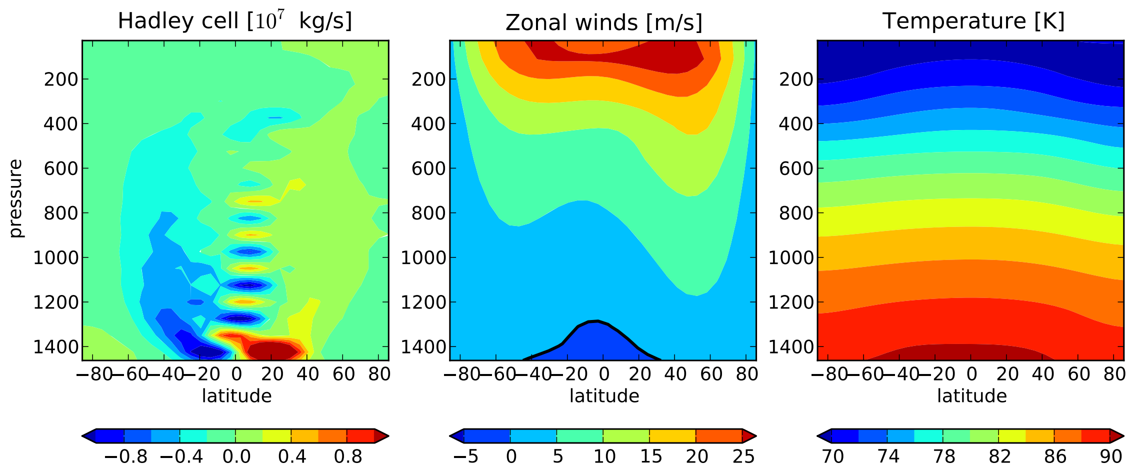

Figure S4: Zonal mean fields averaged over an 1800-day model integration started just before northern spring equinox. *Left:* The mass flux of the Hadley circulation [10^7 kg/s], with positive (negative) colors indicating clockwise (counter-clockwise) circulation. *Middle:* Zonal winds with the zero-wind-line marked in bold. Note that robust tropospheric superrotation is achieved, as evidenced by prograde (positive) winds directly over the equator (the stratosphere is not well-resolved in our model). *Right:* Temperature.

Figure S4 displays the zonal- and time-mean Hadley cell (left) zonal winds (center) and temperature (right) for the 1800-terrestrial-day integration bracketing northern spring equinox used in the main text. We draw attention to the fact the model produces robust superrotation in the troposphere, with peak winds exceeding 20 m/s as observed (the stratosphere is not well resolved).

3 Tests for convective coupling

Figure S5 shows the logarithms of power spectra of the surface zonal wind (left column) and precipitation (right column) for 1000 days of our model simulation near northern spring equinox and averaged between 70N/S latitudes (top row). The wind spectrum is dominated by eastward-propagating waves (positive wavenumbers), particularly at wavenumber two and a frequency of $\sim$0.12 days^{-1}.On the westward-propagating (negative wavenumbers) side, a much slower group of disturbances is evident and dominated by wavenumber two. These two features account for the majority of the precipitation, as seen by comparison with the top-right panel.

We also show in Figure S5 two test case simulations carried out over the same timeframe as the standard case. In the first case (middle row), we have fixed the surface wind used to diagnose surface heat fluxes rather than allowing the winds to be self-consistently diagnosed from the model atmosphere. This test is aimed at discriminating a particular type of evaporation-wind feedback [16, 17]. The eastward-propagating wave is unaffected, while the westward wave is substantially altered, particularly in the precipitation field. In the second test (bottom row), we remove the latent heating entirely by setting the latent heat of vaporization to zero. This test gives qualitatively similar results to the previous one. We conclude the westward-propagating wave is convectively coupled while the eastward-propagating wave is not. The eastward-propagating wave clearly has a strong organizing influence on the pattern of precipitating convection, but latent heating does not influence it.

4 Spatial structure and nature of simulated tropical waves

The method used to isolate the structure of the dominant modes of tropical variability in the simulations involves 3 steps:

1. The surface zonal wind field is filtered using a top-hat spectral filter retaining zonal wavenumbers and frequencies within a range centered on a chosen spectral feature. Specifically, two filtered datasets are produced: one retaining zonal wavenumbers 1–4 and eastward-propagating frequencies 0.06–0.22 day^{-1} (periods 4.5–17 days), and another retaining the same zonal wavenumbers and westward-propagating frequencies 0.002–0.06 day^{-1} (periods 17–500 days).

2. EOF analysis is applied to each of the filtered surface wind datasets. In the presence of zonally-propagating waves, EOF analysis gives two leading modes with the same explained variance and structure, but shifted 90° out of phase in the zonal direction. The principal components (PCs) associated with these 2 degenerate modes are lagged in phase, yielding a zonally-propagating pattern. Lag-correlation of the 2 PCs gives peak correlation at a lag equal to 1/4 of the wave's period. We find peaks at a lag of 2 and 25 days for the eastward- and westward-filtered datasets respectively, matching the spectral peaks at 8 and 100 days seen in Fig. 1.

3. The PC associated with one of the 2 leading EOFs from each dataset is then regressed onto the raw (unfiltered) simulation output to yield the three-dimensional structure of anomalies associated with each of the modes.

Results are shown in Figure S6. The eastward mode (top row) has a horizontal structure closely matching a shallow water equatorially-trapped Kelvin wave of zonal wavenumber 2 [18]. Vertically, the mode fills the troposphere, defined as the layer between about 400 hPa and the ground embraced by moist convection and the Hadley cell (Fig. 1). It is highly baroclinic, with 4 sign reversals in the zonal wind anomaly from top to bottom. Linear theory predicts a phase speed $c = N/m$, where N is the Brunt-Väisälä frequency and $m = 2\pi n/H$, with n the vertical wavenumber and H the depth of the mode. Taking $N \approx 3 \times 10^{-3}$ s^{-1}, $n = 2$ and $H \approx 26$ km gives $c \approx 6.5$ m s^{-1}. Adding an eastward Doppler shift of 3.5 m s^{-1}, corresponding to the depth-averaged zonal-mean zonal wind in the layer yields a total phase speed of about 10 m s^{-1}, in good agreement with the actual phase speed seen in the simulation.

The westward mode (Figure S6, bottom row) fills a shallow layer between about 1300 hPa and the ground. This layer is dry-adiabatic, with a jump at its top to the higher static stability of the moist convective layer. Horizontally, the mode is a combination of zonal wavenumbers 1 and 2 and is confined to—and fills—the Southern Hemisphere. The mode is not an obvious match to any of the equatorially-trapped modes of shallow water theory. It may arise through the interaction of phase-locked equatorial and high-latitude modes, as seen in previous theoretical work [19].

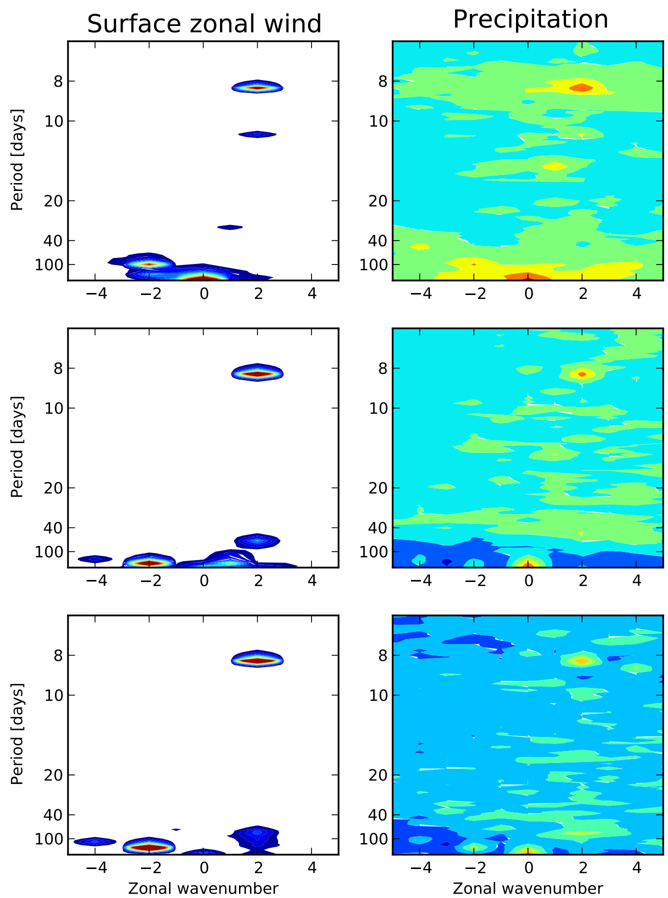

Figure S5: Wavenumber-frequency power spectra of surface zonal winds (left) and precipitation (right) for 1000 days near northern spring equinox of our simulations. The top row is our standard case analyzed in the main text. The middle and bottom rows display the no-evaporation-wind feedback test case and the zero-latent-heating test case, respectively (see text for more discussion). A slow, westward-propagating mode with a period of 100 days is present in the standard case, but it is substantially altered in the two test cases, indicating it is a convectively coupled wave. The strongest eastward-propagating mode at wavenumber 2 and frequency 0.12 day^{-1} is present in all cases, indicating it is not convectively coupled.

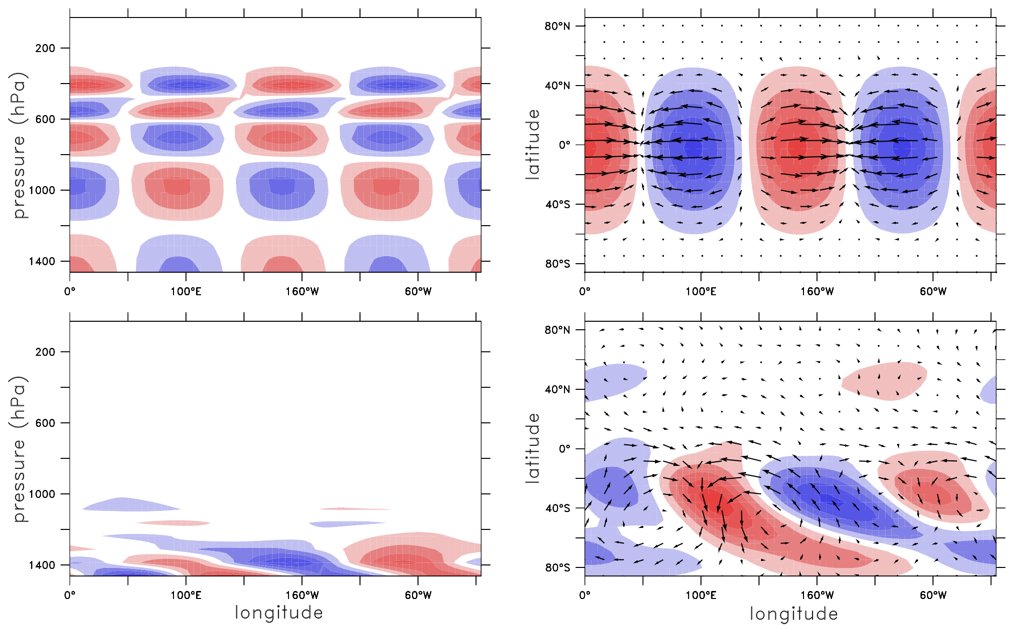

Figure S6: Spatial structure of the leading eastward (top row) and westward (bottom row) modes of variability. Left column shows an equatorial cross section of the zonal wind anomaly (red positive, blue negative). Right column shows horizontal structure of the geopotential height anomaly (shading) and wind (arrows) at 1000 hPa (top) and 1400 hPa (bottom).

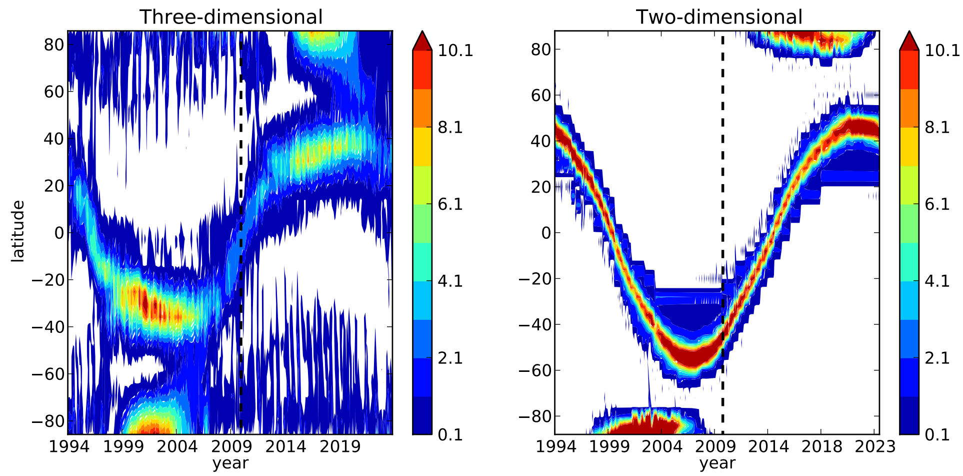

Figure S7: Zonal-mean precipitation rate normalized to the global- and annual-mean rate (a) during one simulated Titan year of our GCM and (b) from the two-dimensional "moist" simulation of [20]. The location of the northern spring equinox is marked by a dashed line.

5 Diagnostics of methane precipitation and evaporation

Figure S7 displays the zonal-mean precipitation rate normalized to the global- and annual-mean rate for our three-dimensional GCM (a) and two-dimensional simulation (b) [20]. The equatorial chevrons are associated with the most intense zonal-mean equatorial precipitation during the equinoctial transition, which is marked by the dashed line. These are ephemeral.

Figure S8 shows the global- and annual-mean methane transport of our GCM, with positive (negative) values indicating northward (southward) transport. The region between 10°S and 10°N latitudes experiences net divergence of transport, indicating climatological surface evaporation there. The ephemeral equatorial precipitation associated with chevrons in Figure S7 do not produce net accumulation.

Figure S9 shows a space-time diagram of the model precipitation rate averaged between 10°S to 20°S latitudes at a time corresponding to early 2008, roughly the location and time of the cloud outburst observed by [21]. The eastward-propagating mode has a phase speed of roughly 8 m/s (solid line), which is in agreement with the Kelvin mode associated at a later model epoch with the equatorial chevron. The dashed line indicates 3 m/s, which was the observed propagation speed. The superposition of the Kelvin mode (symmetric about the equator) and the southern-hemisphere ITCZ produces the eastward-propagating precipitation features.

Figure S10 displays precipitation rates and surface wind anomalies during a sequence of approximately 3 terrestrial years bracketing NSE. The non-axisymmetric precipitation features are concentrated at low latitudes, and show a clear progression from the south to the north with time.

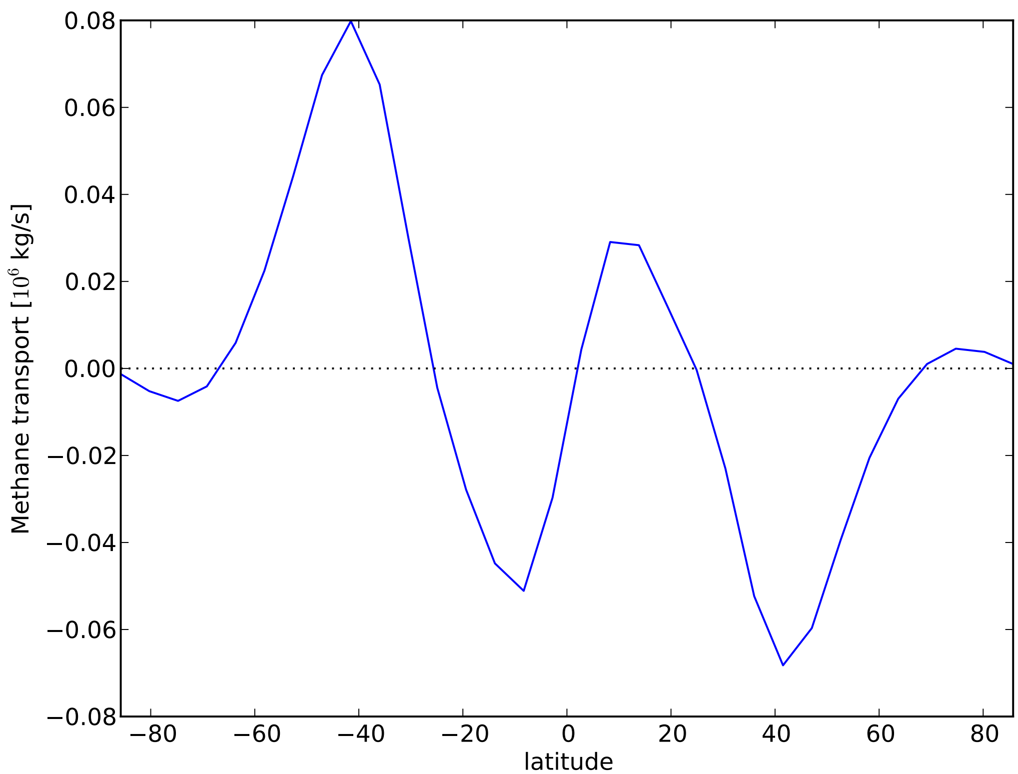

Figure S8: Global- and annual-mean methane transport by the atmosphere in our GCM. The region bounded by 10°S and 10°N latitudes experiences net divergence of methane transport, indicating the surface experiences net evaporation.

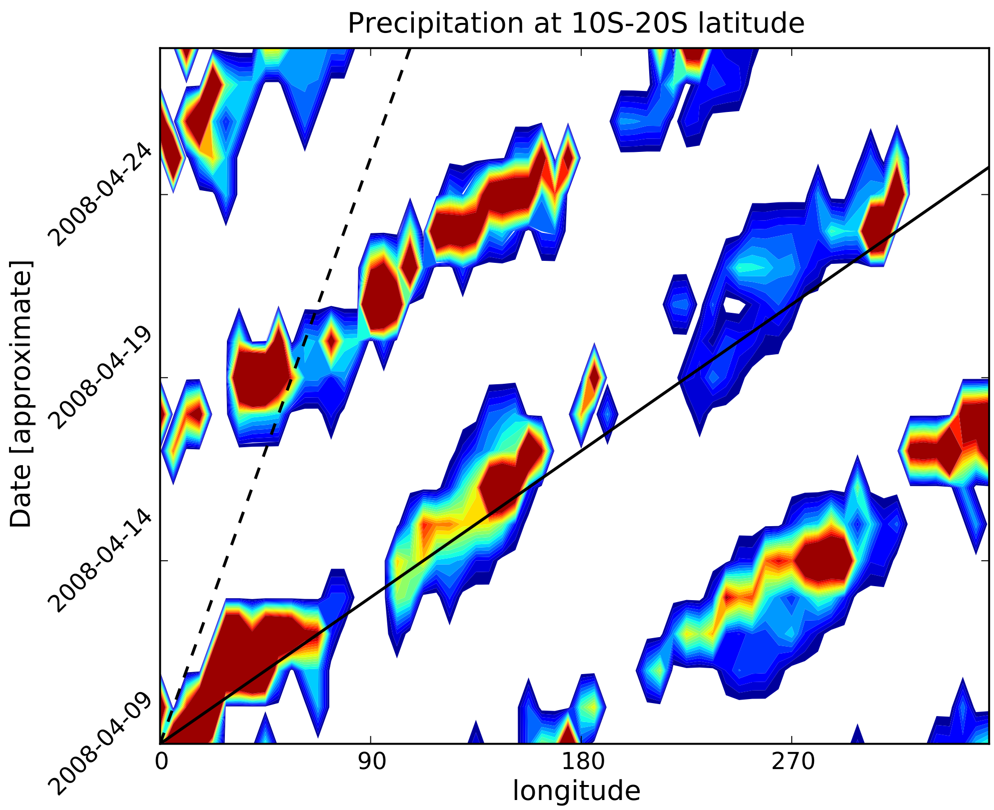

Figure S9: Space-time diagram of precipitation averaged between 10°S to 20°S latitude during the epoch observed by [21]. The solid line indicates eastward motion at 8 m/s and the dashed line is eastward at 3 m/s.

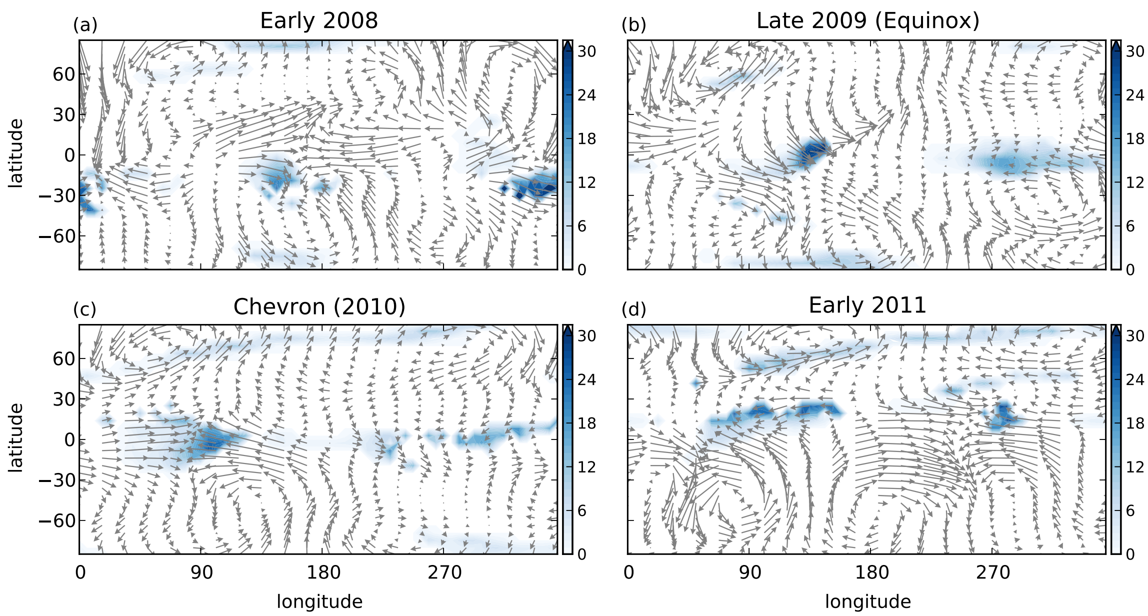

Figure S10: Time sequence of precipitation rate (blue, normalized to the global- and time-mean rate) and surface wind anomalies (arrows) during a 3-terrestrial-year epoch bracketing NSE.

References

[1] Ádámkovics, M., De Pater, I., Hartung, M. & Barnes, J. Evidence for condensed-phase methane enhancement over Xanadu on Titan. *Planetary and Space Science* **57**, 1586–1595 (2009).

[2] Ádámkovics, M., Barnes, J., Hartung, M. & de Pater, I. Observations of a stationary mid-latitude cloud system on Titan. *Icarus* **208**, 868–877 (2010).

[3] Karkoschka, E. & Tomasko, M. Methane absorption coefficients for the jovian planets from laboratory, Huygens, and HST data. *Icarus* **205**, 674–694 (2010).

[4] Tomasko, M. *et al.* Measurements of methane absorption by the descent imager/spectral radiometer (DISR) during its descent through Titan's atmosphere. *Planetary and Space Science* **56**, 669–707 (2008).

[5] Turtle, E. *et al.* Seasonal changes in Titan's meteorology. *Geophys. Res. Lett.* **38**, L03203 (2011).

[6] Barth, E. & Toon, B. O. Methane, ethane, and mixed clouds in Titan's atmosphere: Properties derived from microphysical modeling. *Icarus* **182**, 230–250 (2006).

[7] Samuelson, R. E. & Mayo, L. A. Steady-state model for methane condensation in titan's troposphere. *Planetary and Space Science* **45**, 949–958 (1997). URL `http://www.sciencedirect.com/science/article/pii/S0032063397000895`.

[8] Whalley, E. & McLaurin, G. E. Refraction halos in the solar system. i. halos from cubic crystals that may occur in atmospheres in the solar system. *J. Opt. Soc. Am. A* **1**, 1166–1170 (1984). URL `http://josaa.osa.org/abstract.cfm?URI=josaa-1-12-1166`.

[9] Tokano, T. *et al.* Methane drizzle on Titan. *Nature* **442**, 432–435 (2006).

[10] Barth, E. L. & Toon, O. B. Microphysical modeling of ethane ice clouds in titan's atmosphere. *Icarus* **162**, 94–113 (2003). URL `http://www.sciencedirect.com/science/article/pii/S0019103502000672`.

[11] Mitchell, J., Pierrehumbert, R., Frierson, D. & Caballero, R. The impact of methane thermodynamics on seasonal convection and circulation in a model Titan atmosphere. *Icarus* **203**, 250–264 (2009).

[12] Gordon, C. & Stern, W. A description of the GFDL global spectral model. *Mon. Wea. Rev* **110**, 625–644 (1982).

[13] McKay, C., Pollack, J. & Courtin, R. The greenhouse and antigreenhouse effects on Titan. *Science* **253**, 1118–1121 (1991).

[14] Frierson, D. M. W., Held, I. M. & Zurita-Gotor, P. A gray-radiation aquaplanet moist GCM. Part I: Static stability and eddy scale. *Journal of the Atmospheric Sciences* **63**, 2548–2566 (2006).

[15] Tokano, T. Meteorological assessment of the surface temperatures on Titan: constraints on the surface type. *Icarus* **173**, 222–242 (2005).

[16] Emanuel, K. An air-sea interaction model of intraseasonal oscillations in the tropics. *Journal of the Atmospheric Sciences* **44**, 2324–2340 (1987).

[17] Neelin, J. & Held, I. Modeling tropical convergence based on the moist static energy budget. *Monthly Weather Review* **115**, 3–12 (1987).

[18] Matsuno, T. Quasi-geostrophic motions in the equatorial area. *J. Meteor. Soc. Japan* **44**, 25–42 (1966).

[19] Mitchell, J. & Vallis, G. The transition to superrotation in terrestrial atmospheres. *J. Geophys. Res.* **115**, E12008 (2010).

[20] Mitchell, J., Pierrehumbert, R., Frierson, D. & Caballero, R. The dynamics behind Titan's methane clouds. *Proc. Natl. Acad. Sci. USA* **103**, 18421—18426 (2006).

[21] Schaller, E., Roe, H., Schneider, T. & Brown, M. Storms in the tropics of Titan. *Nature* **460**, 873–875 (2009).